Chemical Science

RSC Publishing

EDGE ARTICLE

View Article Online
View Journal | View Issue

Open Access Article. Published on 03 April 2013. Downloaded on 8/21/2024 6:42:43 AM.
This article is licensed under a Creative Commons Attribution 3.0 Unported Licence.

Cite this: *Chem. Sci.*, 2013, **4**, 2403

Epitaxial growth and enhanced conductivity of an IT-SOFC cathode based on a complex perovskite superstructure with six distinct cation sites†

R. Sayers,[a] N. L. O. Flack,[a] J. Alaria,[a] P. A. Chater,[a] R. G. Palgrave,[a] S. R. C. McMitchell,[a] S. Romani,[b] Q. M. Ramasse,[c] T. J. Pennycook[cd] and M. J. Rosseinsky*[a]

Received 7th November 2012
Accepted 1st April 2013

DOI: 10.1039/c3sc21931c

www.rsc.org/chemicalscience

Epitaxial thin films of the 10 layer cubic perovskite superstructure $Ba_{1.7}Ca_{2.4}Y_{0.9}Fe_5O_{13}$ were grown by pulsed laser deposition, retaining the six distinct cation sites found in the bulk material. Growth on single crystal strontium titanate (STO) (0 0 1) substrates changes the observed symmetry from orthorhombic to tetragonal and orients the layer stacking direction of the superstructure normal to the substrate plane. The material is a candidate cathode for solid oxide fuel cells (SOFCs) and in the intermediate temperature (IT) region at 600 °C we measure the in-plane AC conductivity of the thin film as 30 S cm^{-1}, significantly enhanced over 3.5 S cm^{-1} found for the polycrystalline form. This is assigned to reduction of the grain boundary density and alignment of the planes predicted to have the highest electronic and ionic conductivities. High resolution electron microscopy measurements demonstrate the atomic site ordering producing the superstructure and reveal defects associated with stacking faults in the ordering sequence.

Introduction

Solid oxide fuel cells (SOFCs) are of great interest in the sustainable energy area because of their potentially high output efficiency and their fuel flexibility.[1,2] Intermediate temperature (IT-) SOFCs operate at temperatures in the region of 550 °C to 750 °C, where the thermal demands on the system components are less challenging than those for high temperature SOFCs operating at *circa* 900 °C.[3] In an effort to achieve these lower operating temperatures, materials for SOFC cathodes are required to have high ionic and electronic conductivities as well as good thermal stability in this intermediate temperature range.[4] One approach to enhancing the conductivity of these materials is through growth in thin film form which is proposed for micro-IT-SOFC applications.[1,5] By studying thin films of materials which have previously been characterized and shown promising behaviour in the polycrystalline bulk form, significant improvements in the electrical properties can be observed for simple perovskite-based materials (Fig. 1(a)).[1] Epitaxial films of $La_{0.8}Sr_{0.2}CoO_{3-\delta}$ (LSC) grown by pulsed laser deposition (PLD) show dramatically enhanced oxygen reduction activity over the bulk material,[6] and microelectrode based devices can be grown.[7] By studying thin films of the perovskite $BaZr_{0.8}Y_{0.2}O_{3-\delta}$, Pergolesi *et al.*[8] find that the proton conductivity is significantly enhanced in textured oriented thin films compared with the bulk due to the absence of blocking grain boundaries. In addition to the impact of microstructural differences between films and bulk on the properties, thin film growth can optimise the properties of anisotropically structured materials where there are preferred structural pathways for ion and electron transport. The A site cation ordering in the double

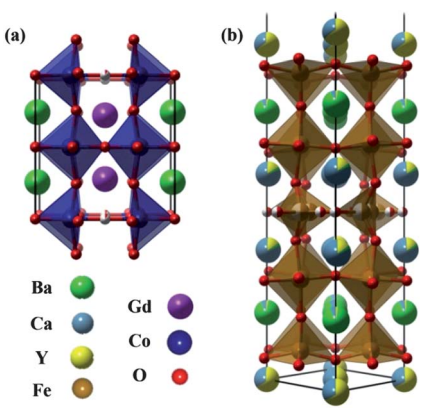

Fig. 1 Crystal structures of (a) $GdBaCo_2O_{5.5}$ and (b) $Ba_{1.7}Ca_{2.4}Y_{0.9}Fe_5O_{13}$. Fractionally occupied sites are shown as part white.

[a]*Department of Chemistry, University of Liverpool, Liverpool, L69 7ZD, UK. E-mail: rossein@liverpool.ac.uk*

[b]*Nanoinvestigation Centre at Liverpool (NiCaL), Department of Engineering, The University of Liverpool, Waterhouse Building, Block C, 1-3 Brownlow Street, Liverpool, L69 3GL, UK*

[c]*SuperSTEM Laboratory, STFC Daresbury Campus, Keckwick Lane, Daresbury WA4 4AD, UK*

[d]*Department of Materials, University of Oxford, Parks Road, Oxford OX1 3PH, UK*

† Electronic supplementary information (ESI) available. See DOI: 10.1039/c3sc21931c

Open Access Article. Published on 03 April 2013. Downloaded on 8/21/2024 6:42:43 AM.
This article is licensed under a Creative Commons Attribution 3.0 Unported Licence.

perovskites $LnBaCo_2O_{5+\delta}$ (Ln = lanthanide) (Fig. 1(a)) creates high ionic mobility for oxide anions within the Ln-containing anion vacancy layers, resulting in highly anisotropic oxide anion mobilities in crystals[9] and thin films.[10–13] The A site ordering strategy thus creates anisotropic materials with properties that would be suitable for enhancement through oriented growth in thin film as opposed to bulk ceramic form.

Recently the new IT-SOFC cathode material $Ba_{1.7}Ca_{2.4}Y_{0.9}Fe_5O_{13}$ has been reported with a perovskite-based, cation ordered, layered structure.[14] $Ba_{1.7}Ca_{2.4}Y_{0.9}Fe_5O_{13}$ can be described as a regular intergrowth between $Ca_2Fe_2O_5$ and $YBa_2Fe_3O_8$ building blocks leading to a complex superstructure displaying 20 times the unit-cell volume of a classic cubic perovskite (Fig. 1(b)). $Ba_{1.7}Ca_{2.4}Y_{0.9}Fe_5O_{13}$ belongs to the orthorhombic space group *Imam*, and has bulk lattice parameters $a = 5.50$ Å, $b = 5.54$ Å, and $c = 38.20$ Å, with the c axis corresponding to a ten-layer ($10a_p$) repeat of the basic cubic perovskite cell. Throughout this paper we use the non-standard setting *Imam* to describe the crystal structure in order to have the c axis the long axis which is more conventional to describe thin films of layered materials. There are six distinct cation sites (3 perovskite A sites and 3 B sites) describing this complex material. The eight-coordinated A site is predominantly occupied by Y^{3+}, the nine-coordinated site by Ca^{2+} and the 12-coordinated site by Ba^{2+} and Fe is present in three unique B site co-ordination environments, namely tetrahedral, square based pyramidal and octahedral; the ordering of these cations leads to a layered structure in which partially oxygen deficient layers allow oxygen ion transport. Here we describe the composition of the films deposited using the nominal stoichiometry of the target ($Ba_{1.7}Ca_{2.4}Y_{0.9}Fe_5O_{13}$). A study on the experimentally determined cation ratios to obtain this layered and ordered structure free from impurities has been previously made by Demont *et al.*,[14] where a nominal cation stoichiometry of $Ba_{1.7}Ca_{2.4}Y_{0.9}Fe_5$ was found to give a phase pure material.

Cathodes of $Ba_{1.7}Ca_{2.4}Y_{0.9}Fe_5O_{13}$ have an area specific resistance (ASR) of 0.87 Ω cm^2 at 700 °C,[14] and with optimization of the microstructure this has been lowered to 0.24 Ω cm^2 suggesting that they are candidates for IT-SOFC applications. This electrochemical behaviour is combined with excellent thermal stability in air and under a CO_2 atmosphere, as well as chemical stability and a good thermal expansion match with the $Ce_{0.8}Sm_{0.2}O_{2-\delta}$ electrolyte. The electronic conductivity of the bulk ceramic is notably low compared with Co-containing materials such as $La_{0.6}Sr_{0.4}Co_{0.2}Fe_{0.8}O_{3-\delta}$ (LSCF), LSC and the $LnBaCo_2O_5$ systems.[15] Density functional theory (DFT) calculations on the $10a_p$ Fe-based material show that it is expected to have highly anisotropic conductivity behaviour as the 3d-bandwidth and thus the electronic conductivity should be strongly enhanced in the *ab* plane.[14] This suggests the growth of this SOFC cathode in thin film form, in order to exploit the complex A cation ordering-based superstructure to enhance the properties over the bulk ceramic material. PLD has previously proven effective at depositing high order Aurivillius and Ruddlesden-Popper structures with large out-of-plane lattice parameters from a single target.[16–18] The plasma arriving at the substrate will be homogeneous in composition, so the growth of such films requires the reorganisation of atoms in the out-of-plane direction on the scale of the unit cells of these materials, which can equal several nanometres. Since the growth rate in PLD is typically on the order of 1 nm per minute, this reorganisation must occur after condensation of the plasma on the substrate, happening behind the growth front, and driven by an energetically favourable long range order. In contrast the in-plane epitaxial organisation (over much shorter length scales) occurs on the order of milliseconds.[19] Here we report the growth of $Ba_{1.7}Ca_{2.4}Y_{0.9}Fe_5O_{13}$ films which show the expected bulk cation ordering from a single target of that composition. This requires the deposition of a material with six distinct cation sites in an ordered, oriented manner to retain the favourable structural characteristics of the parent polycrystalline ceramic. We also report the multiple lengthscale structural evaluation and electrical property characterization of these films.

Experimental section

$Ba_{1.7}Ca_{2.4}Y_{0.9}Fe_5O_{13}$ ($10a_p$) thin films were deposited on (0 0 1)-$SrTiO_3$ (STO) substrates by PLD with a KrF COMPeX Pro Lambda Physik excimer laser with $\lambda = 248$ nm. A dense pellet (90% of the theoretical density) of the $10a_p$ compound was prepared following the procedure described by Demont *et al.*[14] The growth conditions were optimized by varying the growth temperature from 750–950 °C and X-ray diffraction (XRD) patterns from this temperature range are shown in Fig. S1(a),† with 850 °C being the optimal deposition temperature. The effect of the laser fluence on the formation of a competing structure with a smaller $3a_p$ unit cell was investigated. Additional $3a_p$ diffraction peaks in the XRD patterns were observed when the fluence was 0.30 J cm^{-2} or 0.24 J cm^{-2}. An optimal fluence of 0.27 J cm^{-2} was found to avoid formation of this competing phase. The partial pressure of oxygen was not altered; 1 mTorr produced single phase films. The optimised growth conditions were found to be a deposition temperature of 850 °C with a laser fluence of 0.27 J cm^{-2}, a frequency of 5 Hz, pO_2 of 1 mTorr. After deposition, the oxygen pressure was set to 150 Torr, and the substrate heater was turned off to rapidly cool the sample from the deposition temperature to room temperature in approximately 10 minutes.

XRD including rocking curves (RC) and reciprocal space maps (RSM), and X-ray reflectivity (XRR), were carried out using a Philips X'Pert diffractometer equipped with a Cu K_α X-ray source (λ = 0.15419 nm) and a four bounce Ge monochromator. The out-of-plane and in-plane lattice parameters were determined by measuring appropriate diffraction peaks using either coupled symmetrical $\theta/2\theta$ scans or by measuring RSMs. The deposition rate of the $10a_p$ films was obtained by measuring XRR on a series of thin films grown with various numbers of pulses. At the optimized growth conditions stated above, the growth rate was found to be 333 pulses per nanometre. As will be shown *infra*, the structure is orientated with the c axis in the out-of-plane direction, and so this growth rate corresponds to 1295 pulses per unit cell. A film with a thickness of 90 nm was grown for AC impedance measurements with 30 000 pulses.

 This journal is © The Royal Society of Chemistry 2013

Open Access Article. Published on 03 April 2013. Downloaded on 8/21/2024 6:42:43 AM.
This article is licensed under a Creative Commons Attribution 3.0 Unported Licence.

AC impedance spectroscopy was conducted in 2-probe in-plane geometry; sputtered gold electrodes were used for the contacts, with gold wires attached using a small spot of gold paste. The gold paste was dried at 200 °C for 2 hours in air, with a heating and cooling rate of 3 °C min^{-1}. The film was then heated slowly at 3 °C min^{-1} to 600 °C in oxygen and AC impedance measurements were made on cooling to 200 °C. The conductivity was measured over the frequency range 0.01 Hz to 1 MHz, and in the temperature range 200 °C to 600 °C in flowing oxygen (1 atm O_2). A Solartron 1260 FRA in conjunction with a Solartron 1296 dielectric interface with SMaRT software was used to carry out the measurements and the collected data was analysed using the *Z*-view software (Scribner Associates). The thin film was left to equilibrate at temperature for 90 minutes prior to each conductivity measurement.

In order to compare the thin film and the polycrystalline conductivity from the same starting materials, 4-point DC conductivity was performed on rod-shaped polycrystalline bulk samples of 98% relative density obtained from the material used to make the PLD target. Platinum wire was used for the electrodes (attached using a very small amount of platinum paste) and annealed at 800 °C for 1 hour before starting the measurement. The bulk ceramic was left to equilibrate at temperature for at least 120 minutes prior to each conductivity measurement and the resistances used were seen to be stable over the equilibration time.

Aberration corrected Scanning Transmission Electron Microscopy (STEM) was performed on a JEOL 2100 FCs, with Schottky electron source. A CEOS GmbH hexapole corrector provided reduction of the spherical aberration of the probe forming system to less than 10 μm. The beam convergence semi-angle was maintained at 20 mrad, with camera lengths of either 12 cm or 8 cm, providing High Angle Annular Dark Field (HAADF) images with collection semi angle ranges of approximately 54–145 mrad and 74–196 mrad, respectively.

Further STEM and electron energy loss spectroscopy (EELS) measurements were performed on a Nion UltraSTEM operated at 100 keV primary beam energy using a cold field emission electron source, a corrector capable of neutralizing up to fifth order aberrations[20] and a Gatan Enfina EEL spectrometer. The probe forming optics were configured to deliver a probe convergence semi-angle of 31 mrad, while the EELS collection semi-angle was calibrated at 36 mrad. The HAADF detector collection semi-angle range was 85–195 mrad for *Z*-contrast imaging. Although in these operating conditions the native energy spread of the beam is 0.35 eV, the spectrometer dispersion was set up to acquire simultaneously a wide range of edges and its resolution was thus limited by the detector point spread function at about 1.4 eV. The principle component analysis (PCA) method[21] was used to reduce noise in atomic-resolution EELS elemental maps as described by Varela *et al.*[22]

Results and discussion

A typical $\theta/2\theta$ X-ray diffraction pattern of a $10a_p$ film grown under optimised conditions is shown in Fig. 2. All peaks have been assigned Miller indices which show that the film grows with the

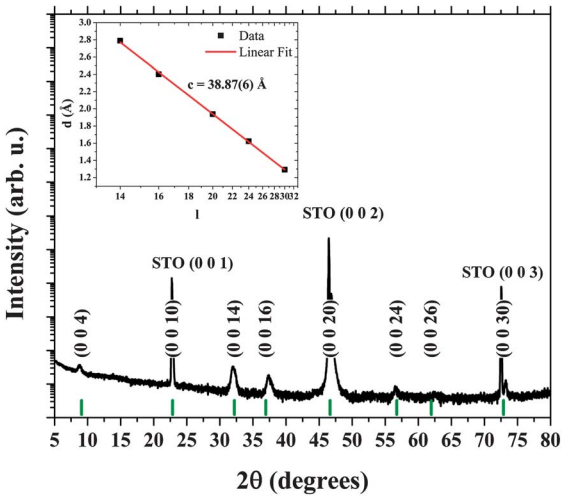

Fig. 2 XRD pattern of an optimised $10a_p$ film deposited on (0 0 1) STO. The green vertical lines correspond to the expected $10a_p$ (0 0 *l*) reflections from the calculated *c* parameter. The (0 0 1) STO peak is to the left of the (0 0 10) $10a_p$ peak and is hidden beneath the inset. The inset shows the *d*-spacing of the film's reflection as a function of its indices and the least square fit used to determine the out-of-plane lattice parameter.

$10a_p$ long axis perpendicular to the plane of the STO (0 0 1) substrate. The observation of the (0 0 4) peak with *d*-spacing of 10.04 Å in the diffraction pattern shown in Fig. 2 is a clear indication of the long range ordering within the $10a_p$ material (the (0 0 2) peak would be observed below the lowest 2θ angle measured in this study). Bragg peaks from (0 0 6), (0 0 8) and (0 0 12) reflections are not observed (see Table S1†), although comparison with the simulated powder diffraction pattern of the crystal structure shows that these reflections are weaker than the (0 0 4), (0 0 14) and (0 0 16) reflections that are clearly observed. The long axis of the $10a_p$ structure was assigned as the *c* axis and the out-of-plane lattice parameter was calculated using all the reflections as presented in the inset of Fig. 2 and was found to be 38.87(6) Å. This value is larger than the reported bulk value (38.20 Å) which is possibly due to the presence of oxygen vacancies or to a strain effect. The $10a_p$ material gives a minimal compressive lattice mismatch when grown at 45° on a (0 0 1) STO substrate. Considering the $\sqrt{2} \times \sqrt{2} \times 10a_p$ superstructure of this compound, an in-plane 45° rotation with respect to the STO lattice is expected, producing a strain of −0.5% and +0.4% in the (1 1 0) and (1 $\bar{1}$ 0) substrate directions. Conservation of the bulk volume and a completely strained film in both axes would result in a decrease of the out-of-plane lattice parameter to 38.17 Å. The observed increase in *c* parameter to 38.87(6) therefore cannot be entirely explained by epitaxial strain. Given the accurate cation stoichiometry to be shown *infra*, the slight increase in *c* parameter is likely caused by oxygen deficiency, commonly seen in PLD films grown at reduced pressure.[23]

A typical XRR scan from a pure $10a_p$ film is shown in Fig. 3(a), and the observation of Kiessig fringes is indicative of a film with sharp interfaces. IMD software[24] was used to model the experimental data. The reflectivity calculated on the basis of the structural model match well with the experimental data and the thickness (~36 nm) and roughness (0.7 nm) can be

Open Access Article. Published on 03 April 2013. Downloaded on 8/21/2024 6:42:43 AM.
This article is licensed under a Creative Commons Attribution 3.0 Unported Licence.

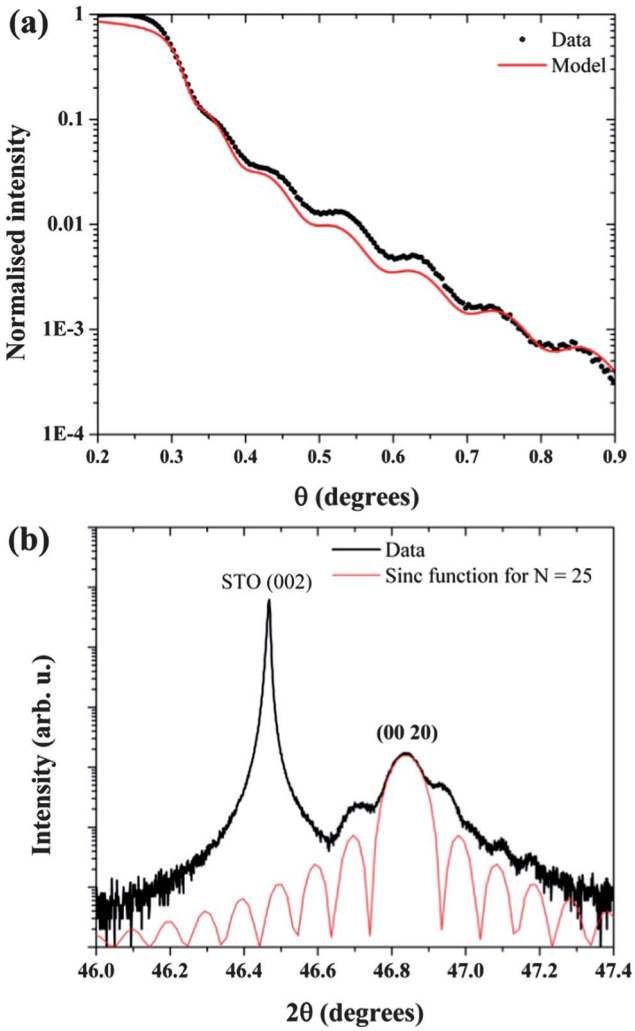

Fig. 3 (a) XRR of a 36 nm 10a_p film, experimental data in black, with the calculated reflectivity in red, (b) HRXRD around the (0 0 20) 10a_p Bragg peak of a 95 nm films showing Pendellosung fringes and a simulated crystal truncation rod for 25 monolayers.

extracted. The small roughness obtained (corresponding to approximately two cubic perovskite subcells) is an indicator of high quality growth with no island formation. Further support for the high coherence between the substrate and the film can be found in Fig. 3(b) with Pendellosung fringes clearly evidenced around the (0 0 20) Bragg peak of a thicker film. The period of the Pendellosung fringes can be used to determine the thickness of the film using the sinc function. The red curve on Fig. 3(b) corresponds to 25 monolayers of the 10a_p (~95 nm) structure and matches well to the experimental data.

To confirm the epitaxial quality of the 10a_p films grown by this protocol, rocking curves were measured on the thickest film. Fig. 4(a) shows full width half maxima (FWHMs) of 8.2 × 10^{-3} degrees for the STO substrate. The observed shoulder on the STO rocking curve is due to the presence of slightly misoriented twin crystals and is commonly observed in STO substrates.[25] The rocking curve of the 10a_p (0 0 20) reflection displayed in Fig. 4(b) has a FWHM of 2.9 × 10^{-2} degrees, and a similar shoulder to that observed for the substrate, indicating that the film grows oriented onto each twin. The high degree of crystalline quality is emphasized by the narrowness of each peak. In comparison Taskin *et al.*[9] report the FWHM of single crystal $GdBaCo_2O_{5.5}$ as less than 0.1° and Kasper *et al.* report the FWHM of ~2° for $TbBaCo_2O_{6-\delta}$ films grown by PLD.[26] The rocking curve peak width measured on the 10a_p film is the narrowest reported for these A site ordered layered perovskite-based compounds and indicates the high degree of uniformity and structural perfection of the grown films.

Texture studies were also carried out on the 10a_p films by measuring pole figures using the (1 1 2) reflection of STO, Fig. 5(a), and the (2 0 20) of the 10a_p film in Fig. 5(b). The (2 0 20) reflection of the 10a_p was selected since it has a relatively large structure factor and would give a clear picture on the twinning state of the sample. Both pole figures have a 4-fold symmetry which is expected for the STO substrate. A 2-fold symmetry is expected for the 10a_p film assuming the orthorhombic symmetry of the bulk phase, although the degree of orthorhombic distortion is small ($b/a = 1.009$). There are several explanations which can be offered for the observed 4-fold symmetry, as set out schematically in Fig. S2.† The first contributing factor is a 90° twinning of the crystal in-plane which would result in an additional pair of peaks which are likely to overlap given the small orthorhombic distortion of the bulk phase. Secondly the low resolution used for the

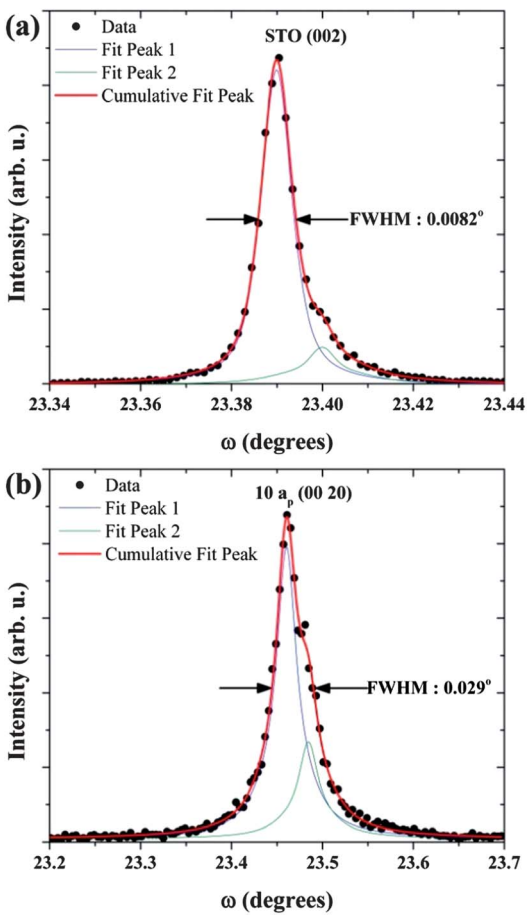

Fig. 4 Rocking curves of (a) the STO substrate and (b) the 95 nm 10a_p film.

This journal is © The Royal Society of Chemistry 2013

Open Access Article. Published on 03 April 2013. Downloaded on 8/21/2024 6:42:43 AM.
This article is licensed under a Creative Commons Attribution 3.0 Unported Licence.

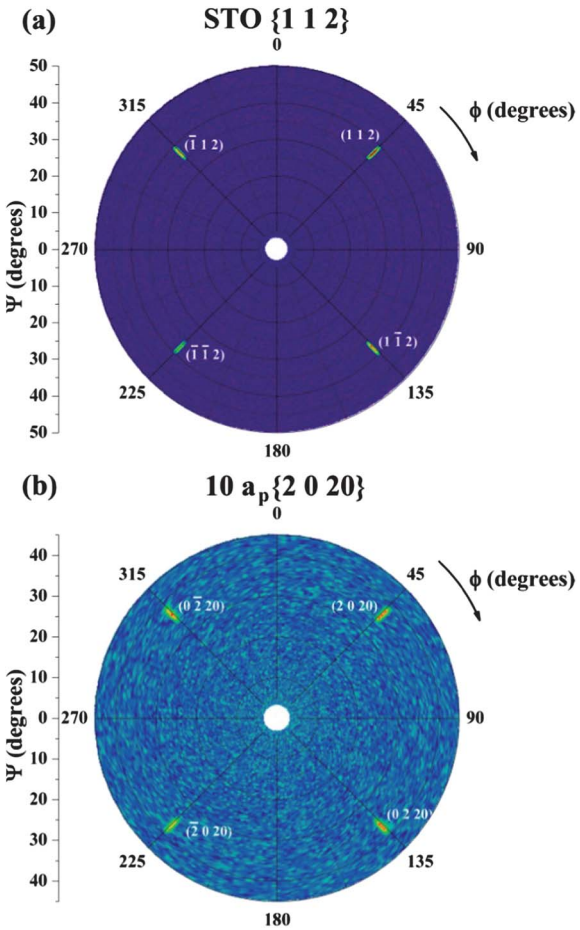

Fig. 5 Pole figure of (a) the (1 1 2) STO substrate reflection and (b) the (2 0 20) reflection of the 10a_p film.

measurement, and the small difference in *d*-spacing between the non-equivalent (2 0 20) and the (0 2 20) reflections would result in an apparent 4-fold symmetry. The structure factors calculated from the bulk crystal structure of those two reflections are very similar, as are the observed intensities in the pole figures, so the observed intensities cannot be used to differentiate between the reflections. The last explanation would be a change of symmetry from orthorhombic to tetragonal due to the in-plane structural match. It is probable that there is a combination of all of these effects, with a reduction in orthorhombic distortion due to the in-plane structural match, coupled with 90° twinning of the structure, giving rise to a separation of (2 0 20) and (0 2 20) which is not resolvable given the instrumental resolution.

To confirm the potential epitaxial relationship between the substrate and the film, and the in-plane symmetry of the film, high resolution X-ray diffraction measurements were performed. Fig. 6(b) shows a RSM of the STO (0 0 2) and the 10 layer (0 0 20) reflections. It can be seen that the substrate and film peaks are vertically aligned, confirming the growth direction as the long axis of the 10a_p unit cell as well as the low mosaicity of the film. To obtain information on the in-plane lattice parameter asymmetric RSMs were measured around the STO (1 1 2) and the (1 $\bar{1}$ 2) reflections as presented in Fig. 6(a) and (c). This RSM data for the film would be expected to be non-equivalent if the symmetry was orthorhombically distorted like the bulk phase, with slightly different Q_x values for the film peaks (0.364 Å^{-1} and 0.361 Å^{-1} for the (2 0 20) and (0 2 20) reflections respectively). However, both in-plane lattice parameters are found to be equivalent with a value of $a_T = 5.48(3)$ Å, leading to the assignment of tetragonal symmetry within the resolution of the measurement, explaining the apparent 4-fold symmetry observed in the pole figure. The epitaxial relationship shows the film grows with a 45° rotation in plane to align the perovskite subcell parameters of the film with the STO perovskite unit cell as illustrated in Fig. S2.† The small orthorhombic distortion observed in the bulk ($c/a = 1.009$) is not observed within the error of the measurements employed for the thin film grown on a cubic substrate. It has previously been noted that $TbMnO_3$, which adopts an orthorhombic unit cell in the bulk ($a/c = 1.113$), gives a suppressed orthorhombic distortion when grown as a thin film on cubic STO;[27] it is probable that a similar suppression in orthorhombic distortion also occurs for the 10a_p thin film grown on cubic STO, although the relatively small orthorhombic distortion of bulk 10a_p means that this could not be confirmed within the resolution of our measurements.

The epitaxial growth of the thin film can be seen in the HAADF STEM image shown in Fig. 7(a). The STO substrate appears in the top right corner of this *Z*-contrast image, and can be identified by the interpenetrating cubic sublattices of the brighter Sr and darker TiO columns. Tracing rows of atomic

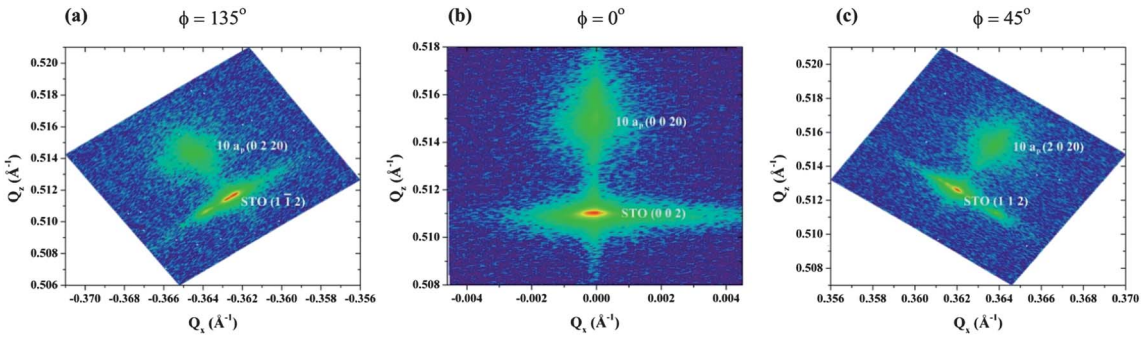

Fig. 6 RSM of the STO substrate and the 10a_p film. (a) Around the (0 2 20) reflection (b) around the (0 0 20) reflection, (c) around the (2 0 20) reflection. The (0 2 20) and (2 0 20) peaks show equivalent Q_x values, leading to the assignment of tetragonal symmetry within the resolution of the measurement.

Open Access Article. Published on 03 April 2013. Downloaded on 8/21/2024 6:42:43 AM.
This article is licensed under a Creative Commons Attribution 3.0 Unported Licence.

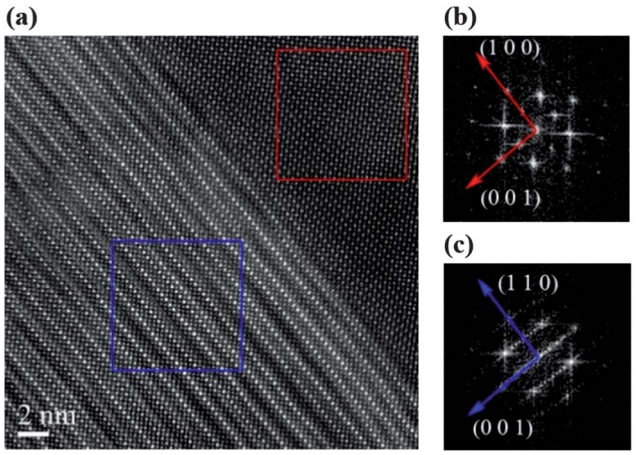

Fig. 7 (a) HAADF STEM image (8 cm camera length) showing the interface between the $10a_p$ film and the STO substrate. Fast Fourier transform (FFT) images of the substrate (b) and film (c).

columns diagonally from the top right perpendicularly across the interface in this image, one can see the interface is coherent. Every one of these rows of columns continues from inside the STO, straight across the interface and all the way through the film visible in the image. The FFTs of both the substrate and film shown in (b) and (c) respectively can be used to determine the zone axis, which is found to be $(1\ \bar{1}\ 0)$ for the $10a_p$ film, and (0 1 0) for the STO substrate, confirming the 45° rotation of the film in-plane and the growth direction. The 10 layer periodicity can be seen in Fig. 7(c) with the five expected superstructure reflections from the body-centred ten layer superstructure observed along the (0 0 1) axis.

The complex layered structure of the material is shown in detail in Fig. 8. The HAADF STEM image in Fig. 8(a) was filtered using an annular mask in the FFT of the raw image to remove environmental noise sources. The qualitative information remains intact, with the higher localized intensities indicative of higher average atomic number in the associated atom column along the beam direction. The registration of higher and lower Z atom rows with the structural model, shown alongside Fig. 8(a), provides a clear match to the entire unit cell. Five types of atomic columns are expected: $Ba_{0.90}Ca_{0.08}Y_{0.02}$, $Ca_{0.34}Y_{0.66}$, $Ba_{0.05}Ca_{0.80}Y_{0.15}$, FeO and pure O columns with average atomic numbers of 52.78, 32.54, 24.65, 17 and 8 respectively. As the intensity in the HAADF images varies roughly as the square of the atomic number, there should be significant contrast between the different layers. Fig. 8(a) shows, horizontal rows of the brightest atomic columns bounding layers containing either 3 or 5 rows of less intense columns, creating 4 row building blocks ($Ca_2Fe_2O_5$) and 6 row ($YBa_2Fe_3O_8$-like) building blocks respectively. The 10 layer unit cell is highlighted in blue. Blurring of two sets of atom columns within the experimental image in Fig. 8(a) is due to disorder associated with the Fe^{3+} tetrahedral layer, as depicted in the structural schematic (purple polyhedra) and confirmed in Fig. 8(b), which shows a simulated HAADF-STEM image using the computer program QSTEM.[28]

Defects can be seen in the HAADF image shown in Fig. 8(c). On the left side of this image the intensities of the columns are consistent with the expected 10 layer stacking continuing for at least 5 unit cells starting from the top of the image. However, the majority of the rows in this image starting with very high intensity on the left do not maintain that intensity much more than halfway across the image to the right. Most often, the row becomes less intense on the right side, and the row below it takes on the high intensity corresponding to the Ba rich columns. Using the width between successive rows of the brightest columns as a guide, it appears the steps often correspond to a change from the one kind of building block on the left to the other. The layering on the right side of the image is

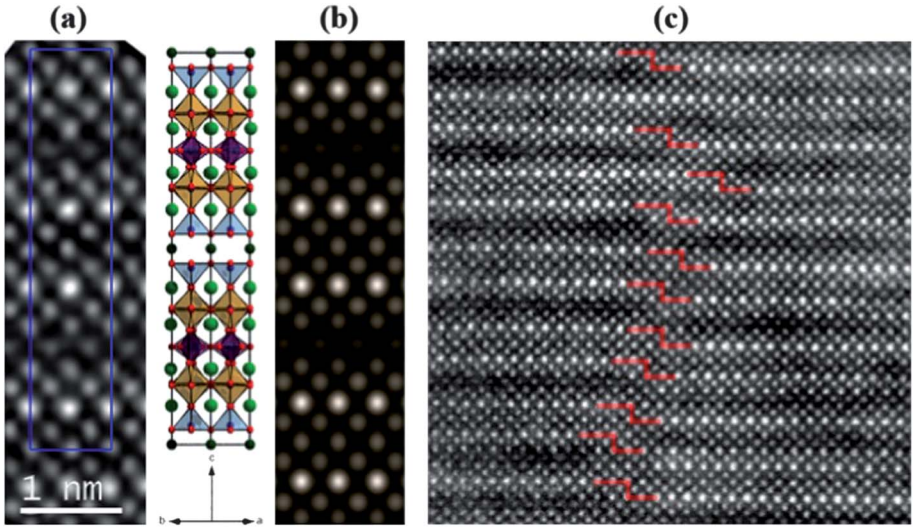

Fig. 8 (a) FFT filtered HAADF STEM image (12 cm CL, JEOL 2100 FCs), with a scaled structural schematic of the $10a_p$ unit cell alongside. An unfiltered version of this image is shown in Fig. S3 (a) and (b)† simulated HAADF-STEM image viewed down the (0 1 0) direction of the $10a_p$ unit cell, (c) wider view showing stacking fault of one atomic step in the 10 layer sequence (indicated by red lines) – this image was collected on the Nion UltraSTEM.

This journal is © The Royal Society of Chemistry 2013

Open Access Article. Published on 03 April 2013. Downloaded on 8/21/2024 6:42:43 AM.
This article is licensed under a Creative Commons Attribution 3.0 Unported Licence.

harder to determine in general though, perhaps due to the propagation of the stacking fault through the thickness of the sample. The perovskite structure is maintained over long distances however, with the defects appearing to affect the occupation of the sites in the crystal rather than their general arrangement. These step-like defects can be assigned to steps in the substrate and also the presence of mixed surface SrO and TiO_2 surface terminations, which will change the initial layer in the perovskite superstructure from BO_2 to AO respectively.

EELS spectrum imaging was performed to determine the chemical identities of the columns forming the 10 layer structure. Spectra were acquired in a 70 by 280 pixel grid across the region indicated by the yellow box in Fig. 9(a) with an acquisition time of 0.01 seconds per pixel. The HAADF signal was recorded simultaneously with each spectrum, forming the *Z*-contrast image shown in Fig. S3(b).† The image facilitates an accurate spatial registration of the elemental maps. Some elongations and distortions can be seen in the image due to sample drift, but the individual atomic columns are clearly resolved. Fig. 9(b) through (e) map the intensities of the Ba M_{45}, Ca L_{23}, Y M_{45} and Fe L_{23} EELS edges respectively. The final map shown in Fig. 9(f) is a colour overlay of the individual maps, with the green, red, blue and yellow channels representing the respective Ba, Ca, Y and Fe intensities. The spectra were acquired by scanning from left to right in rows starting from the top of the yellow box in Fig. 9(a) and progressing down one pixel at a time. As can be seen by the presence of elongated atoms in the HAADF image acquired during the acquisition of the spectrum image, the sample drifted downwards in the plane of the image during the acquisition. Because of the drift, the lattice seen in the spectrum image is stretched in this direction.

Fig. 9(g) displays a model of the structure based on refined structure of the bulk material, scaled to match the magnification of the EELS map. The atoms in the model have been coloured to indicate the overall occupation of each type of site throughout the material rather than to indicate the precise locations of any dopant atoms.

The correct proportions have been used in the model, so the model and the maps do not align perfectly along the whole length from top to bottom due to the spatial drift of the microscope during acquisition. It is, however, clear from the side-by-side comparison of the model and the composite map that the expected 10 layer ordering is present in the thin film. The first row of atomic columns at the top of the spectrum image appear among the brightest in the HAADF image, and EELS indicates they are indeed Ba rich, showing strongly green in the composite map, consistent with their identification as $Ba_{0.90}Ca_{0.08}Y_{0.02}$ columns. Following these are a row of Fe rich columns, then a row of columns rich in both Ca and Y, then another row of Fe rich columns completing the first 4 layer building block of the ten layer structure. As Ca shows in the red channel and Y in the blue channel in the composite map, the fact that the columns containing both in this first 4 layer building block appear dark purple is consistent with the expectation that these columns are $Ca_{0.34}Y_{0.66}$. The second 6 row building block of the 10 layer structure can be seen to follow the first building block as expected with a bright green Ba rich row followed by three rows of yellow Fe rich columns interspersed by 2 rows of columns appearing mostly red, but with some areas of light purple, consistent with what one would expect for $Ba_{0.05}Ca_{0.80}Y_{0.15}$.

After the first 10 layers, two more repeats of 10 layers appear in the spectrum image consistent with the expected structure, with drift the only major cause of mismatch between the model and the composite map. The last few rows appearing in the spectrum image, however, are less straightforward to identify and can be associated with defects within the stacking sequence. After the last row of the third set of 10 layers are the expected rows of green columns followed by a dark purple row of atoms sandwiched between two rows of yellow columns. Rather than the next row having the expected strong green colour, however, it appears only weakly green containing a significant amount of red. The Ca map shows a weak pair of rows of columns with roughly equal intensity at the bottom of the spectrum image as one sees in the 6 layer building blocks

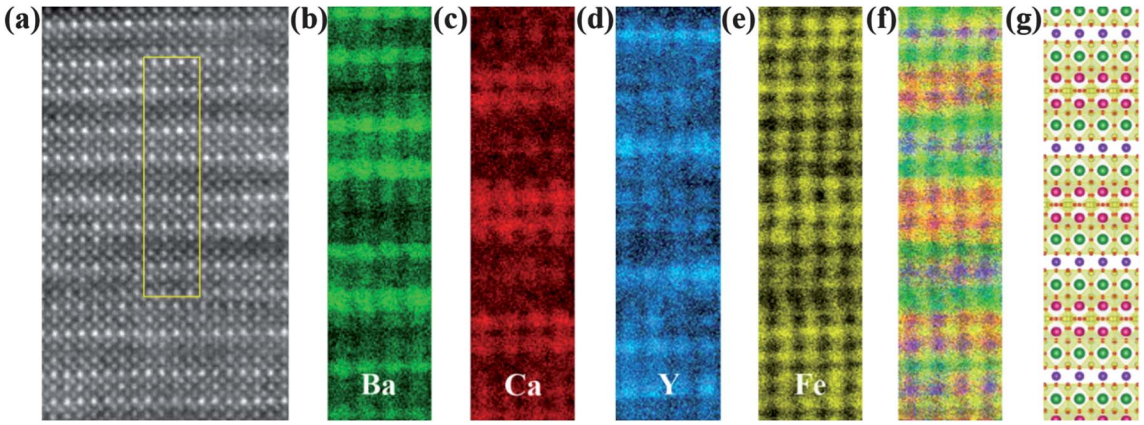

Fig. 9 Atomic resolution *Z*-contrast STEM images and elemental maps. Spectra were acquired in a 70 by 280 pixel grid in the region indicated by the yellow box in survey image (a), with an acquisition time of 0.01 seconds per spectrum. (b)–(e) represent the EELS maps of Ba M_{45}, Ca L_{23}, Y M_{45} and Fe L_{23}, respectively. (f) Colour overlay of the individual maps, with green, red, blue and yellow channels representing Ba, Ca, Y and Fe, respectively. (g) Scaled structural model of the $10a_p$ unit cell. The colours were chosen to match that which one would expect to see in the composite EELS map for a given type of cation column according to the refined cation site occupancies.

Open Access Article. Published on 03 April 2013. Downloaded on 8/21/2024 6:42:43 AM.
This article is licensed under a Creative Commons Attribution 3.0 Unported Licence.

of the 10 layer structure. The top of these two rows of Ca rich columns also appear rich in Y. The bottom row of Ca containing columns also appears as a row of medium intensity columns in the Ba map. The columns are still well defined in the images, so this could be a case of intermixing between the layers. It could also be that a stacking fault exists at this point of the sample, such that looking down this axis of the crystal, at some depths the expected 10 layer stacking continues with another 4 row building block but at other depths another 6 row building block follows the previous one.

The total conductivity of the same nominal composition material was measured in flowing oxygen for a bulk sample (using the 4-probe DC technique) and for the epitaxial thin films (using a 2-point AC technique). AC impedance measurements were undertaken on the 90 nm film to measure the in-plane total conductivity of the $10a_p$ film. The Nyquist plots of the AC impedance cooling data are shown in Fig. 10(a); the conductivities are calculated from the low frequency intercept of the *x*-axis; on increasing temperature the resistance (intercept) decreased, showing thermally activated conductivity in films of the mixed ionic electronic conductor (MIEC), as expected. In an effort to elucidate the conductivity processes present in the thin film, attempts were made to fit the impedance arcs using an equivalent circuit model (ECM); typical Nyquist plots and fitting of the AC impedance data at a selection of temperatures are shown in Fig. 10(a). The impedance response could be separated into three distinct regions; high, medium and low frequency (see ECM shown in inset of Fig. 10(a)). From consideration of the observed low polarisation and the scattering phenomena at low frequency (LF) below 1×10^4 Hz, this response is assigned to the gold contact electrodes.[29] A response of this nature is also observed at low frequencies for Au contacts deposited in the same orientation as that used here when measuring thin films of $Ce_{0.8}Sm_{0.2}O_{2-\delta}$.[30] The remaining parts of the Nyquist plot are composed of two overlapping depressed arcs in the high to mid frequency region (10^7 to 10^4 Hz). The arc observed at high frequency (HF) (10^7 to 10^6 Hz) displayed a characteristic capacitance of the order of 10^{-11} F and the best fit to this arc was achieved by a resistor (R_1) and constant phase element (CPE_1) in parallel with one another. The CPE is used to model the capacitance of an arc with a depressed angle *i.e.* when the impedance response does not belong to a perfect capacitor. The arc fitted to the mid-frequency (MF) range (10^6 to 10^4 Hz) was also modelled by a resistor (R_2) and constant phase element (CPE_2) in parallel with one another and the fitted capacitance of this arc is 10^{-12} F. The resistance associated with the high frequency arc was consistently smaller than that of the arc in the mid-frequency range, indicating that the conductivity process associated with the mid-frequency contributes the larger resistance to the total conductivity. In polycrystalline materials, the high frequency arc is associated with conductivity in the bulk (capacitance of 10^{-12} F), whilst the lower frequency arc is assigned to grain boundary conductivity (capacitance of 10^{-11} to 10^{-8} F), whereas in single crystals or thin films without grain boundaries, the AC impedance response is typically a single arc belonging to the bulk material. In thin films of $Ba_{1.7}Ca_{2.4}Y_{0.9}Fe_5O_{13}$, we observe two overlapping arcs, indicating that there are multiple conduction processes occurring. Given the presence of twinning in the STO substrate, there exists the likelihood of the presence of a small number of grain boundaries in the film, which could contribute to the observed film resistance. This would explain the presence of two overlapping arcs in the high to mid-frequency region, with the HF arc assigned to the bulk response and the MF to the grain boundary response. The HF arc displays a slightly lower capacitance than that of the MF region (10^{-11} F, compared with 10^{-12} F), which is the inverse of what would be expected for a bulk response in the HF region. The reason for this disparity is unknown, however given the relatively small difference in the capacitances as well as the overlapping nature of the HF and MF arcs, separation of the processes is made more complex, and may result in small errors on these values.

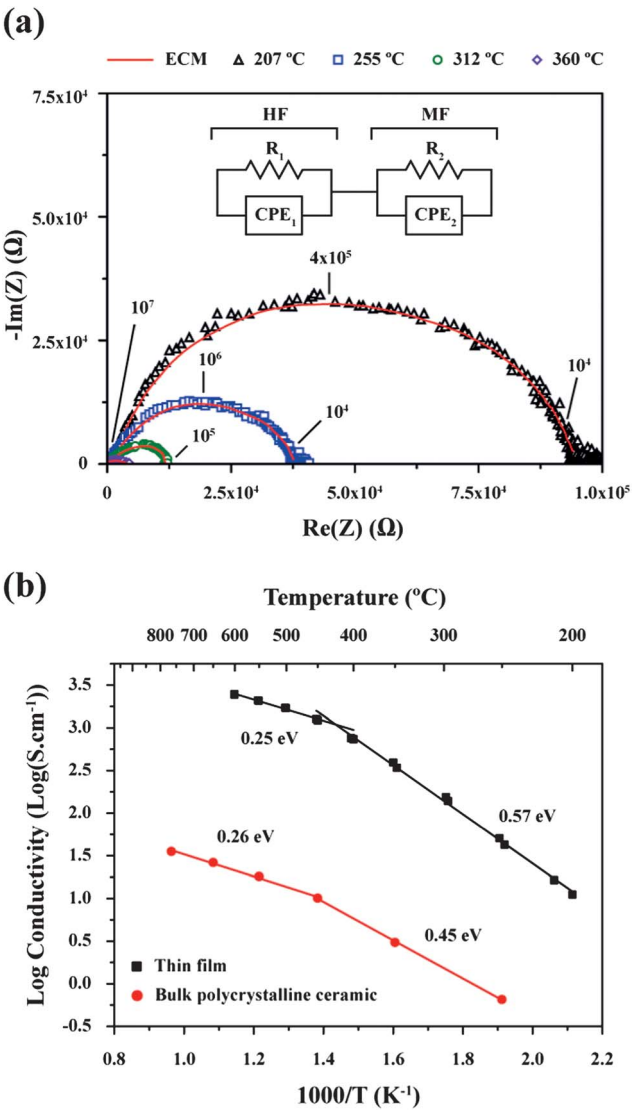

Fig. 10 (a) Experimental arcs, and fits to the equivalent circuit model (ECM) measured at a range of different temperatures, with an inset which shows the ECM for the high frequency (HF) and mid-frequency (MF) arcs. Measured frequency is shown on the Nyquist plot in Hz. (b) Arrhenius plot for conductivity of $10a_p$ bulk polycrystalline ceramic (red circles) and thin film (black squares) as a function of temperature in flowing oxygen. All data shown are on cooling.

This journal is © The Royal Society of Chemistry 2013

Open Access Article. Published on 03 April 2013. Downloaded on 8/21/2024 6:42:43 AM.
This article is licensed under a Creative Commons Attribution 3.0 Unported Licence.

The conductivity as a function of the temperature in an oxygen atmosphere is shown in Fig. 10(b) and Fig. S5(a)† and reaches 30 S cm^{-1} at 600 °C for thin films of $Ba_{1.7}Ca_{2.4}Y_{0.9}Fe_5O_{13}$. Any contribution to the total film conductivity from the STO substrate was taken into account by directly measuring a substrate from the same batch in the same electrode configuration. The STO substrate was found to have a conductivity of the order of 10^{-7} S cm^{-1} at 300 °C and 10^{-3} S cm^{-1} at 600 °C in agreement with the expected values from the literature,[31] and its contribution to the overall measured conductivity is considered negligible. The conductivity of the bulk ceramic in oxygen is 3.5 S cm^{-1} (Fig. 10(b)).

The activation energies for the thin film and polycrystalline sample measured in an O_2 atmosphere are shown on Fig. 10(b), with both samples showing a change in activation energy and displaying low and high temperature regimes. In the thin film, the activation energies are 0.57 and 0.25 eV, for the low (200 °C to 420 °C) and high temperature (420 °C to 600 °C) regimes respectively, with the change in slope occurring in the region of 420 °C. The conductivity of the bulk material also displays two regimes with a transition observed at 450 °C and different activation energies; 0.45 eV (250 °C to 450 °C) and 0.26 eV (450 °C to 765 °C). This clearly shows that the high temperature conductivity is associated with process(es) which display lower activation energy than those at low temperature in both the thin film and the bulk. It also appears that the activated processes in the high temperature regime are the same in the bulk and thin film given the similarity in the activation energies; however the absolute values of conductivity in the thin film are much higher. In the mixed ionic–electronic conductor $Ba_{1.7}Ca_{2.4}Y_{0.9}Fe_5O_{13}$, the total measured conductivity is composed of electronic and ionic components, and the magnitude is dominated by the electronic component (as typical for MIEC materials with ionic conductivity several orders of magnitude lower than the electronic conductivity). The activation energy for conductivity also represents a combination of ionic and electronic components and separation of the contribution from each component to the overall activation energy is complex. The ionic transport as a function of anisotropy of $Ba_{1.7}Ca_{2.4}Y_{0.9}Fe_5O_{13}$ is currently the subject of further detailed study. Demont *et al.*[14] measured the conductivity of dense polycrystalline $Ba_{1.7}Ca_{2.4}Y_{0.9}Fe_5O_{13}$ (nominal stoichiometry) in air and observed two conductivity regimes with the transition in behaviour occurring at approximately 480 °C, at the Néel temperature, coinciding with realignment of Fe^{2+}/Fe^{3+} magnetic spin states. The activation energies were 0.20 eV and 0.11 eV below and above this temperature respectively. We observe a similar transition when measuring in oxygen suggesting a realignment of Fe^{2+}/Fe^{3+} magnetic spin states also occurs when in an oxygen atmosphere.

The band structure indicates that the electronic conduction of ideal composition $Ba_2Ca_2YFe_5O_{13}$ would be dominated by transport along the *a–b* plane and is essentially 2-dimensional in nature.[14] This would explain the enhanced conductivity measured in the oriented thin film of $Ba_{1.7}Ca_{2.4}Y_{0.9}Fe_5O_{13}$, where the electrode configuration leads to measurement along the *a–b* plane compared with the conductivity of a polycrystalline ceramic where the total conductivity is an average over all the randomly oriented grains, that is an average of high transport in the *a–b* plane and reduced transport along the *c*-axis. As $Ba_{1.7}Ca_{2.4}Y_{0.9}Fe_5O_{13}$ is a mixed ionic–electronic conductor, the total conductivity will also have an ionic contribution, however this will be significantly smaller than the electronic contribution; it is therefore not possible to confirm whether oxygen ion conductivity is also enhanced in the oriented thin film and this is the subject of further work. It would, however, be expected that the ionic conductivity would also be enhanced in the direction of the *a–b* plane as there are oxygen deficient layers which will favour oxygen ion transport in this direction.

In addition to the differences in measured directions between the thin film and the bulk materials, there are also microstructural differences which may contribute to the differences in the measured conductivities. The polycrystalline bulk ceramic contains many grain boundaries, whereas the thin film is essentially a single crystal and is almost grain boundary free (the substrate was twinned so a limited number of grain boundaries were present within the film); assuming that the grain boundaries are to some extent blocking for carrier migration then the greatly reduced number in the thin film would also lead to the observed improvements in conductivity.

The reproducibility and stability of the thin film conductivity was verified by cycling of the film over three cooling–heating cycles and is shown in Fig. S5(a) and Table S2.† The stability of these films under the measurement conditions is verified by the observation that there are no changes to the XRD patterns before and after electrical measurement, shown in Fig. S5(b) and (c),† confirming that the lattice parameters remain unchanged and therefore the structure and oxygen stoichiometry are retained. To study the thermal stability of the film a sample was heated to 600 °C at a heating rate of 3 °C min^{-1}; once the film reached 600 °C it dwelled at temperature for 200 hours. No change in the diffraction pattern (Fig. S4†) was observed before and after heating showing that the film is stable for a long period of time at the operating temperature. The stability of the films during the measurement was further verified by studying the conductivity as a function of time (Fig. S6†), it can be seen that there is no significant variation on the conductivity with increasing time during the measurement dwell (90 minutes) over 250 °C to 600 °C. This measured constant conductivity highlights the stability of this phase under the measurement conditions and indicates that there is no competing new phase formation occurring.

Conclusion

The growth of a strongly cation ordered 10 layer perovskite film, with a more complex structure than previous SOFC cathode materials grown in thin film form, has been achieved *via* pulsed laser deposition (PLD). The A site cation composition which produces the 10 layer, six cation site structure in the bulk ceramic also drives the assembly of this complex superstructure when grown as an epitaxial thin film. The symmetry of the film appears to be tetragonal within the resolution of the measurements employed, as opposed to the orthorhombic symmetry of the bulk phase, which may be attributed to the in-plane

Open Access Article. Published on 03 April 2013. Downloaded on 8/21/2024 6:42:43 AM.
This article is licensed under a Creative Commons Attribution 3.0 Unported Licence.

structural match between the cubic STO substrate and the grown layer. This complex structure was confirmed by HRTEM data, which shows the faithful reproduction of the cation site ordering from the bulk material, associated with retention of the A site layering, and the presence of defects associated with faulting in the ordering of the component structural units. The high degree of uniformity and structural perfection of the grown films averaged over larger areas than those probed by TEM was clear from XRD data, with the narrowest rocking curve peak widths thus far reported for ordered layered SOFC cathode candidate materials. The self-assembly of the six-site 39 Å repeat structure derived from the essentially isotropic perovskite subcell in single-target pulsed laser deposition growth reflects the favourable nature of the A site cation ordering which drives the formation of the structure. The perovskite-based nature of the superstructure makes it distinct from large repeat Aurivillius and Ruddlesden-Popper phases which are intrinsically layered due to the insertion of fluorite and rock-salt type layers respectively.

The conductivity of these $10a_p$ films is significantly higher than that of the bulk polycrystalline ceramic. The conductivity attained by the film is 30 S cm^{-1} at 600 °C, greater than that of the bulk 3.5 S cm^{-1}, which is a key temperature for IT SOFCs. The enhanced conductivity is assigned to the reduction in the density of grain boundaries and the *a–b* orientation of the film in-plane. This shows that the electronic conductivity can be increased by oriented growth related to the cation stacking sequence. The film growth has thus revealed good intrinsic transport properties of the complex superstructure $Ba_{1.7}Ca_{2.4}Y_{0.9}Fe_5O_{13}$, as the measured conductivity shows that Fe^{3+}-based oxides can have acceptable conductivities for application as IT-SOFC cathodes.

Acknowledgements

We thank EPSRC for support under EP/H000925, for a studentship to NLOF and for funding SuperSTEM, the National Facility for aberration-corrected scanning transmission electron microscopy.

References

1 J. Santiso and M. Burriel, *J. Solid State Electrochem.*, 2011, **15**, 985–1006.
2 B. C. H. Steele, *Nature*, 1999, **400**, 619–621.
3 N. Q. Minh, *J. Am. Ceram. Soc.*, 1993, **76**, 563–588.
4 C. Sun, R. Hui and J. Roller, *J. Solid State Electrochem.*, 2010, **14**, 1125–1144.
5 D. Beckel, A. Bieberle-Hutter, A. Harvey, A. Infortuna, U. P. Muecke, M. Prestat, J. L. M. Rupp and L. J. Gauckler, *J. Power Sources*, 2007, **173**, 325–345.
6 G. J. la O', S.-J. Ahn, E. Crumlin, Y. Orikasa, M. D. Biegalski, H. M. Christen and Y. Shao-Horn, *Angew. Chem., Int. Ed.*, 2010, **49**, 5344–5347.
7 E. Mutoro, E. J. Crumlin, M. D. Biegalski, H. M. Christen and Y. Shao-Horn, *Energy Environ. Sci.*, 2011, **4**, 3689–3696.
8 D. Pergolesi, E. Fabbri and E. Traversa, *Electrochem. Commun.*, 2010, **12**, 977–980.
9 A. A. Taskin, A. N. Lavrov and Y. Ando, *Phys. Rev. B: Condens. Matter Mater. Phys.*, 2005, **71**, 134414.
10 G. Kim, S. Wang, A. J. Jacobson, L. Reimus, P. Brodersen and C. A. Mims, *J. Mater. Chem.*, 2007, **17**, 2500–2505.
11 Z. Yuan, J. Liu, C. L. Chen, C. H. Wang, X. G. Luo, X. H. Chen, G. T. Kim, D. X. Huang, S. S. Wang, A. J. Jacobson and W. Donner, *Appl. Phys. Lett.*, 2007, **90**, 212111.
12 M. Burriel, M. Casas-Cabanas, J. Zapata, H. Y. Tan, J. Verbeeck, C. Solis, J. Roqueta, S. J. Skinner, J. A. Kilner, G. Van Tendeloo and J. Santiso, *Chem. Mater.*, 2010, **22**, 5512–5520.
13 G. Kim, S. Wang, A. J. Jacobson, Z. Yuan, W. Donner, C. L. Chen, L. Reimus, P. Brodersen and C. A. Mims, *Appl. Phys. Lett.*, 2006, **88**, 024103.
14 A. Demont, M. S. Dyer, R. Sayers, M. F. Thomas, M. Tsiamtsouri, H. N. Niu, G. R. Darling, A. Daoud-Aladine, J. B. Claridge and M. J. Rosseinsky, *Chem. Mater.*, 2010, **22**, 6598–6615.
15 A. Tarancon, M. Burriel, J. Santiso, S. J. Skinner and J. A. Kilner, *J. Mater. Chem.*, 2010, **20**, 3799–3813.
16 J. R. Duclere, M. Guilloux-Viry and A. Perrin, *J. Appl. Crystallogr.*, 2003, **36**, 96–102.
17 M. Matvejeff, K. Yoshimatsu, H. Kumigashira, M. Oshima and M. Lippmaa, *Appl. Phys. Lett.*, 2009, **95**, 152110.
18 M. A. Zurbuchen, N. J. Podraza, J. Schubert, Y. Jia and D. G. Schlom, *Appl. Phys. Lett.*, 2012, **100**, 223109.
19 G. Rijnders, G. Koster, D. H. A. Blank and H. Rogalla, *Appl. Phys. Lett.*, 1997, **70**, 1888–1890.
20 O. L. Krivanek, G. J. Corbin, N. Dellby, B. F. Elston, R. J. Keyse, M. F. Murfitt, C. S. Own, Z. S. Szilagyi and J. W. Woodruff, *Ultramicroscopy*, 2008, **108**, 179–195.
21 M. Bosman, M. Watanabe, D. T. L. Alexander and V. J. Keast, *Ultramicroscopy*, 2006, **106**, 1024–1032.
22 M. Varela, M. P. Oxley, W. Luo, J. Tao, M. Watanabe, A. R. Lupini, S. T. Pantelides and S. J. Pennycook, *Phys. Rev. B: Condens. Matter Mater. Phys.*, 2009, **79**, 085117.
23 T. Ohnishi, K. Shibuya, T. Yamamoto and M. Lippmaa, *J. Appl. Phys.*, 2008, **103**, 103703.
24 D. L. Windt, *Comput. Phys.*, 1998, **12**(1), 226.
25 M. D. Biegalski, D. D. Fong, J. A. Eastman, P. H. Fuoss, S. K. Streiffer, T. Heeg, J. Schubert, W. Tian, C. T. Nelson, X. Q. Pan, M. E. Hawley, M. Bernhagen, P. Reiche, R. Uecker, S. Trolier-McKinstry and D. G. Schlom, *J. Appl. Phys.*, 2008, **104**, 114109–114111.
26 N. V. Kasper, P. Wochner, A. Vigliante, H. Dosch, G. Jakob, H. D. Carstanjen and R. K. Kremer, *J. Appl. Phys.*, 2008, **103**, 013907.
27 C. J. M. Daumont, D. Mannix, V. Sriram, G. Catalan, D. Rubi, B. J. Kooi, J. T. M. D. Hosson and B. Noheda, *J. Phys.: Condens. Matter*, 2009, **21**, 182001.
28 C. T. Koch, Ph.D., Arizona State University, 2002.
29 J. T. S. Irvine, D. C. Sinclair and A. R. West, *Adv. Mater.*, 1990, **2**, 132–138.
30 S. Sanna, V. Esposito, D. Pergolesi, A. Orsini, A. Tebano, S. Licoccia, G. Balestrino and E. Traversa, *Adv. Funct. Mater.*, 2009, **19**, 1713–1719.
31 X. Guo, *Science*, 2009, **324**, 465-a-.

 This journal is © The Royal Society of Chemistry 2013